International Journal of Nanoelectronics and Materials
Volume 13, No. 3, July 2020 [547-564]

High Power Capability of MoS_2 Based Aqueous Electrolyte Supercapacitor

Mohamed H. Mohamedy[1, 2*], M. M. Sayed[1], Ninet M. Ahmed[2], Mohammed B. Zahran[3]

[1]*Electrical Power and Machines Department, Faculty of Engineering, Cairo University, El Giza 12613, Egypt.*
[2]*Photovoltaic Department, Electronics Research Institute, Cairo, 12622, Egypt.*
[3]*National Authority for Remote Sensing and Space Science, Cairo, 1184, Egypt.*

Received 27 April 2020, Revised 13 July 2020, Accepted 18 August 2020

ABSTRACT

This paper aims to develop a high-performance electrode material for supercapacitor applications. A facile hydrothermal, environment-friendly, and low-cost technique was used for synthesizing hexagonal (2H) phase MoS_2. Structural and morphological characterizations were studied using XRD, Raman spectroscopy, SEM, EDX, and HRTEM. The results demonstrate that high-quality flower-like of MoS_2 microsphere that provides a very high surface area has been well synthesized. Symmetric supercapacitors (SCs) based on MoS_2 with Ag-doped reduced graphene oxide (RGO-Ag) additive was fabricated and electrochemically tested using three alkaline hydroxides electrolyte namely NaOH, LiOH, and KOH. The effect of different electrolytes has been investigated using multichannel galvanostats where cyclic voltammetry (CV), galvanostatic charge/discharge (GCD), and electrochemical impedance spectroscopy (EIS) experiments were carried out. Despite the weak alkaline nature of LiOH electrolyte, it reveals convenient electrochemical performances with a relatively large specific capacitance of 120 $F.g^{-1}$ at 5 $mV.s^{-1}$, a high power density of about 20 $KW.Kg^{-1}$, and excellent durability with 90.3 % capacitance retention after more than 10000 cycles. The high-power capability and retention rate of the MoS_2 based SC indicate that it is a candidate material for high-performance SCs applications.

Keywords: Electrolyte Study, Hydrothermal, Layered Material, Mos_2, Nanosheets, Supercapacitor.

1. INTRODUCTION

The primary sources of fossil fuel will eventually deplete as it is non-renewable. Besides that, fossil fuel also causes continuous emission of greenhouse gases, water and air pollution that lead to environmental deterioration and pose a peril to human life. Since several decades, a deep interest in the sources of renewable energy such as hydropower, geothermal, wind, and solar energy has acquired a great interest that helps in fossil resource conservation, limiting carbon dioxide (CO_2) emission and increasing the energy reliability [1]. Renewable energy systems are mainly located in remote areas, and so building power lines that extend till the cities become expensive. Renewable energy resources if available in a concentrated form can be simply stored and transported. To target these issues, developing cutting edge renewable energy storage devices (ESDs) that are scalable, cheap, and environmental friendly will help in far-reaching with encouraging solutions [2]. In this regard, SC is considered one of the promising futuristic ESDs owing to its long cycle life, high power density, and the capability of achieving considerable energy density. Unlike super dielectric double-layer SCs [3], electrochemical SCs are divided into three main types depending on the mechanism of charge storage, electric double layer

*Corresponding Author: *mohamedyali@eri.sci.eg*

capacitance (EDLC) which rely on non-faradic reaction as the ions were accumulated on the electrode surface and no charge transfer between electrode and electrolyte, pseudocapacitors have charge storage mechanism relying on faradic reaction such as redox interactions, involve the transference of ions between electrode and electrolyte, the hybrid type which include the charge storage mechanisms of both faradic and non-faradic [4]. The electrode active material plays a vital role to evaluate the charge storage performance. As yet, numerous materials such as transition metal dichalcogenides, metal oxides, and conducting polymers have been generally scrutinized for synthesizing various types for SCs [5][6][7].

Transition-metal dichalcogenides (TMDC) have distinguished layer structures that make them attract a lot of attention owing to their distinctive chemical and physical properties. They have been utilized in different applications such as SCs, nanoelectronics, catalysis, hydrogen storage, batteries, and water splitting application [8]. As a typical layered TMDC, molybdenum disulphide (MoS_2) has been recently deemed as opportune material for the SC electrode because of its unique layered structure, where a metal Mo layer is sandwiched between two S layers. Those layers are connected together via van der Waal's forces. This structure provides a large surface area and shorter channels for ions transmission, allows the intercalation of the ions from the electrolyte without high deformation of the crystal structure, and provides a pseudocapacitive charge transfer property [9][10][11]. The combination of both EDLCs and pseudocapacitive behaviour makes the MoS_2 as appropriate material for SC. However, the smaller electrical conductivity hinders the charge storage performance of the MoS_2 demanding the addition of conductive additive with higher conductivity or an alternative technique of synthesizing [12]. Many studies have been performed to enhance the performance of MoS_2 by adding various carbon material [13][14] or polymers [15][16][17].

Conductive additives are a small amount of conductive material that needs to be added to the active materials of the prepared electrode to enhance their electrical conductivity. Consequently, enhancement of associated power capability and capitalize their ability of charge storage [18]. The conductive additive was used not only as a conductivity improver but also as charge storage like an electrode active material. Different types of conductive additives have been used and carbon black (CB) is utilized mostly as conductive additive owing to its high electrical conductivity. Though, CB suffers from different shortages such as poor electrochemical performance (<5 $F.g^{-1}$) and relatively low packing density [19]. There are different alternatives for CB such as carbon nano-onion, carbon nanotube, and graphene [20]. Among these materials, graphene has a unique structure that provides it phenomenal mechanical, electrical, and thermal properties [21]. Graphene also has a higher value of specific capacitance when compared with CB. One of the main disadvantages of pure reduced graphene oxide (RGO) is restacking owing to strong Van der Waals force, however, decoration and functionalization could retain this problem [22].

In this work, microspheres flower-like MoS_2 was synthesized by a facile hydrothermal technique. Silver decorated reduced graphene oxide (RGO-Ag) was prepared to be used as conductive additives to enhance the conductivity of the prepared MoS_2. The structure and morphology of the prepared MoS_2 and RGO-Ag have been investigated. Three symmetric SCs based on MoS_2 were fabricated. Three different electrolytes namely KOH, NaOH, and LiOH have been used. The electrochemical performance was examined and discussed.

2. MATERIAL AND METHODS

2.1 Material

Graphite fine powder (98%, CDH.), sodium nitrate $NaNO_3$ (99%, SRL chem.), potassium permanganate $KMnO_4$ (98%, Alfa Aesar), N-Methyl-2-pyrrolidone NMP (99.5 %, SRL chem.), H_2O_2

(30%), hydrochloric acid HCl (36.5-38.0%, Alfa Aesar), sulfuric acid H_2SO_4 (Alfa Aesar), polyvinylidene fluoride PVDF (Alfa Aesar), potassium hydroxide KOH (99.9%, Alfa Aesar), sodium hydroxide NaOH (99.0%, Alfa Aesar), lithium hydroxide LiOH (99.0%, Alfa Aesar), hydrazine hydrate (Sigma-Aldrich), silver nitrate $AgNO_3$ (99.9%, Alfa Aesar), hexaammonium heptamolybdate tetrahydrate $(NH_4)6Mo_7O_{24}$ (99%, SRL chem.) and thiourea CH_4N_2S (99%, SRL chem.). The proposed chemicals were used as delivered without any sort of purification or distillation.

2.2 Preparation of Graphite Oxide (GO)

Graphite oxide (GO) was obtained using the Hummers method [23]. In short, 5 g of graphite and 2.5 g of $NaNO_3$ were added to 115 ml of H_2SO_4. The mixture was then stirred for one hour in an ice bath. $KMNO_4$ was then added very slowly to the mixture to prevent the temperature from exceeding 20°C. The ice bath is then removed, and the mixture was then stirred at a temperature of 40°C for half an hour, and at the end of this process, deionized water (DI) was added slowly. As a next step, 30% H_2O_2 was added very slowly using the dropper to stop the reaction. An extra quantity of DI water was added to the solution. The final mixture was washed by using 5% HCl solution under stirring for two hours to eliminate the metal residues and aged for 48 hours then washed with DI water for 10 times until it reached neutral PH.

2.3 Preparation of RGO-Ag

3 grams of the graphite oxide powder has been suspended in one litre of distilled water for two hours to obtain extremely exfoliated graphene oxide using an ultrasonic probe. The solution of $AgNO_3$ was obtained by adding 0.3 gm of $AgNO_3$ to 30 ml DI water and stirred for several minutes until it became clear. After two hours of GO ultrasonic, the $AgNO_3$ solution was added to exfoliated GO and the ultrasonic probe was used for another 30 minutes. 1 ml of hydrazine hydrate was added, and the beaker was put in a hot water bath at 95°C for four hours. The precipitates was collated and washed for 10 times with DI water and then one time with Ethanol/DI water (50:50) volume ratio. Finally, the collected powder was dehydrated in a vacuum oven at 60°C for 24 hours.

2.4 Preparation of MoS_2

MoS_2 has been synthesized via One-step hydrothermal reaction [24]. $(NH_4)6Mo_7O_{24}$ and CH_4N_2S were used as starting materials. Briefly, 1.55 g of $(NH_4)6Mo_7O_{24}$ and 2.85 g of CH_4N_2S were added to 45 ml of DI water under strong stirring for half an hour to obtain a homogeneous transparent solution. The transparent solution was then moved into a stainless autoclave with a 100 ml Teflon-lined. The autoclave was put inside a muffle furnace. The controller of the heat degree of the furnace was adjusted to 220°C and the time was set to 24 hours. The autoclave was let to cool down naturally to room temperature then black precipitates have been obtained using Whatman filter paper and washed with DI water and ethanol for 10 times. Finally, black precipitates were dehydrated in a vacuum furnace at 60°C for 24 hours.

2.5 Electrode and Cell Preparation

The SC electrodes have been prepared as slurry consisting of 80% MoS_2, 10% RGO-Ag, and 10% PVDF in NMP. A large automatic film coater with a digital adjustable doctor blade is used to coat slurry on graphite foil of 0.1 mm thick. The speed of the film coater is adjusted to 15 mm/s and thickness of the doctor blade to 100 microns then the graphite foil was dehydrated in a vacuum oven at 60°C overnight. Finally, the coated graphite foil was cut into disk shape for SCs assembly and testing. Swagelok type cell shown in Figure 1 was used to test SCs. 5M of three different electrolytes namely NaOH, LiOH, KOH were prepared.

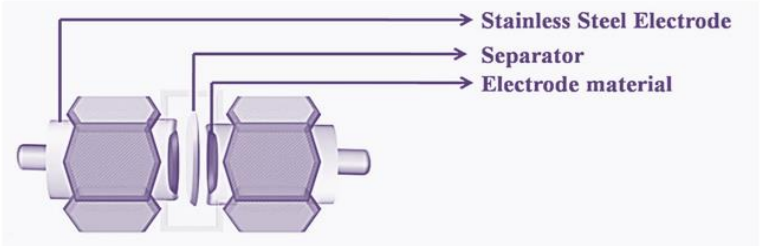

Figure 1. The Swagelok schematic set up for SC cell assembly and testing.

2.6 Electrochemical Measurements

All electrochemical measurements have been done with considering the recommendations of Stoller & Ruoff [25]. A symmetric two electrodes system has been performed to implement the electrochemical characterizations that evaluate the actual SCs performance. The prepared electrodes were put on each side of a glassy carbon separator. The total set up was dipped into the electrolyte. 5M KOH, 5M NaOH, 5M LiOH electrolytes have been used. The electrochemical performance of the SCs was performed using VSP-300 multichannel potentiostat/galvanostat. CV curves were applied in the voltage window of 0 to 1 V at various scan rates (5–100 $mV.s^{-1}$). GCD techniques were applied with different current densities of (0.2 to 10 $A.g^{-1}$) in a voltage window of 0 to 1 V. EIS experiments have been done in the frequency domain from 1 mHz to 2 MHz. The assembled SCs have been examined for 1000 cycles. The specific capacitance (C_{sp}) from CVs was calculated by Eq. (1).

$$Csp = \frac{4\int_{-v}^{+v} I(V)dV}{mVS} \tag{1}$$

Where C_{sp} is the specific capacitance ($F.g^{-1}$), $\int_{-v}^{+v} I(V)dV$ is the area under the CV curve, m is the mass of the electrode active material (gm), [V= V_+ -V_-] the voltage window and S is the rate of scan ($m\ V\ .s^{-1}$).

The specific capacitance of the cell can be obtained from GCD by Eq. (2).

$$Csp = \frac{4I\Delta t}{m\Delta V} \tag{2}$$

Where *I* is the discharge current, Δ*t* is the time of discharge, m is the mass of the electrode active material and Δ*V* represents the operating potential range.

2.7 Characterization Techniques

The crystal structure of MoS_2 and RGO-Ag were studied using X-ray diffraction (Panalytical X'pert PRO MPD X-ray diffractometer) (XRD) with Cu Kα radiation (λ = 0.15418 nm, 30 mA, 40 kV) and dispersive Raman microscope (Pro Raman-L Analyzer) with a laser power of 1 mW and an excitation wavelength of 512 nm. The morphology of the prepared materials was investigated by scanning electron microscope (SEM Model Quanta 250 FEG) and high-resolution transmission electron microscopy (HRTEM, JOEL JEM- 2100).

3. RESULT AND DISCUSSION

3.1 Structure and Morphological Analysis

The crystallinity, structure, and compositions of the synthesized RGO-Ag were affirmed by XRD. Figure 2(a) exhibits the XRD pattern of prepared RGO-Ag. The characteristic diffraction peaks are found at 2θ=37.9°, 44.2°, 64.20° and 77.2° that were attributed to the (111), (200), (220) and (311) silver associated planes, respectively. The deposition of silver nanoparticles (AgNPs) on the RGO nanosheets prohibits the restacking nature of RGO nanosheets. Polycrystalline AgNPs on the RGO nanosheets surface was confirmed by a very sharp intensity of AgNPs diffraction peaks [26]. Moreover, a broad diffraction peak is detected at 2θ = 23.6°, representing the (002) plane of the RGO in the nanocomposites [27]. Figure 2(b) displays the XRD patterns of the prepared MoS_2. The main diffraction peaks of MoS_2 are at 2θ=14.2°, 33.2°, 39.9° and 58.7° that were attributed to the (002), (100), (103) and (110) crystal planes of MoS_2, respectively. The 2H phase of MoS_2 can be indexed which is in agreement with the (JCPDS no. 37-1492) [28]. No diffraction peaks from any additional contaminants have been detected in the XRD pattern, demonstrating the high purity of the prepared MoS_2. Moreover, the formation of a highly stacked layered structure was affirmed by a sharp diffraction peak of (002) of the synthesized MoS_2 with a calculated interlayer spacing of about 0.63 nm.

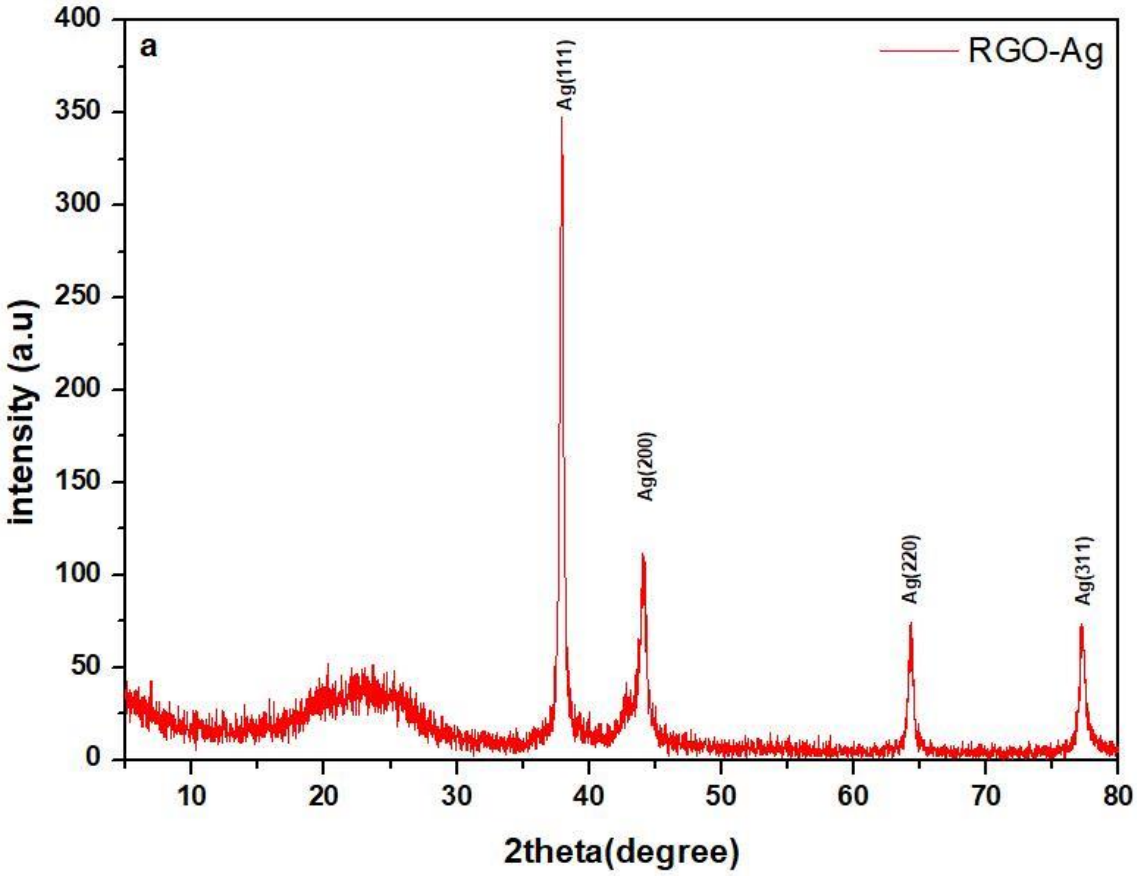

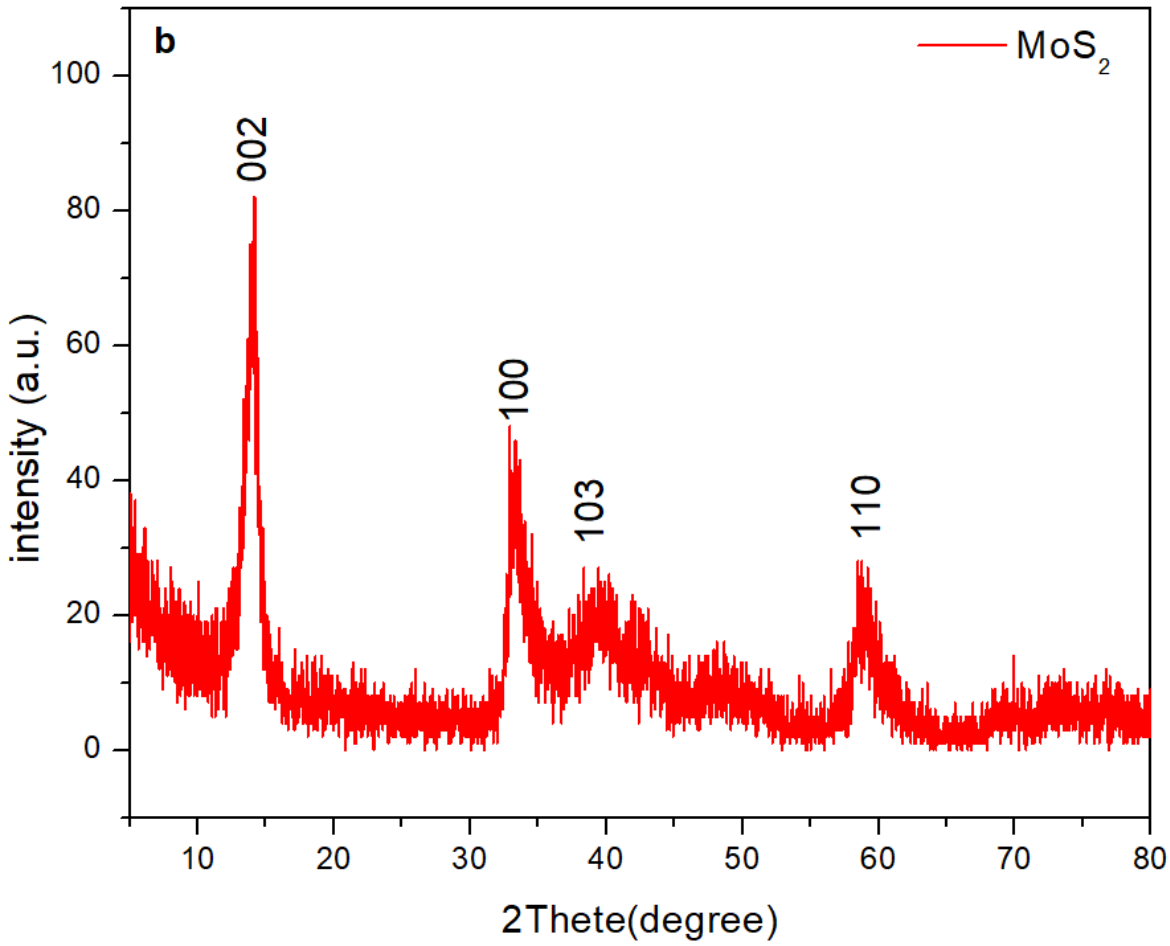

Figure 2. XRD spectrum of synthesized: (a) RGO-Ag, (b) MoS_2.

Raman spectroscopy was used for studying extensive RGO-Ag and MoS_2. In Figure 3(a), the two peaks appeared at 1346 cm^{-1} and 1579.5 cm^{-1} represent the D and G vibration bands of RGO-Ag, respectively. The vibration band of D was created from the breathing mode of j-point phonons of A_{1g} while the G vibration band from the first-order scattering of E_{2g} phonons by sp^2 carbon [29]. The 2D band of RGO-Ag located at 2669-2896.5 cm^{-1} demonstrates that the RGO-Ag comprises of few layers [30]. Figure 3(b) shows the Raman spectrum of MoS_2 which further confirms the formation of MoS_2. The two peaks appeared at 373.5 cm^{-1} (E_{2g}) and 400.5 cm^{-1} (A_{1g}) are attributable to an in-plane and an out-of-plane mode, respectively [31]. The E_{2g} mode relates to an in-plane vibration of Mo and S atoms, whereas the A_{1g} mode correlated with an out-of-plane optical vibration of the S atoms [32]. The stronger and sharper peaks of E_{2g} and A_{1g} indicating the polycrystalline structure of MoS_2 which confirms the XRD results.

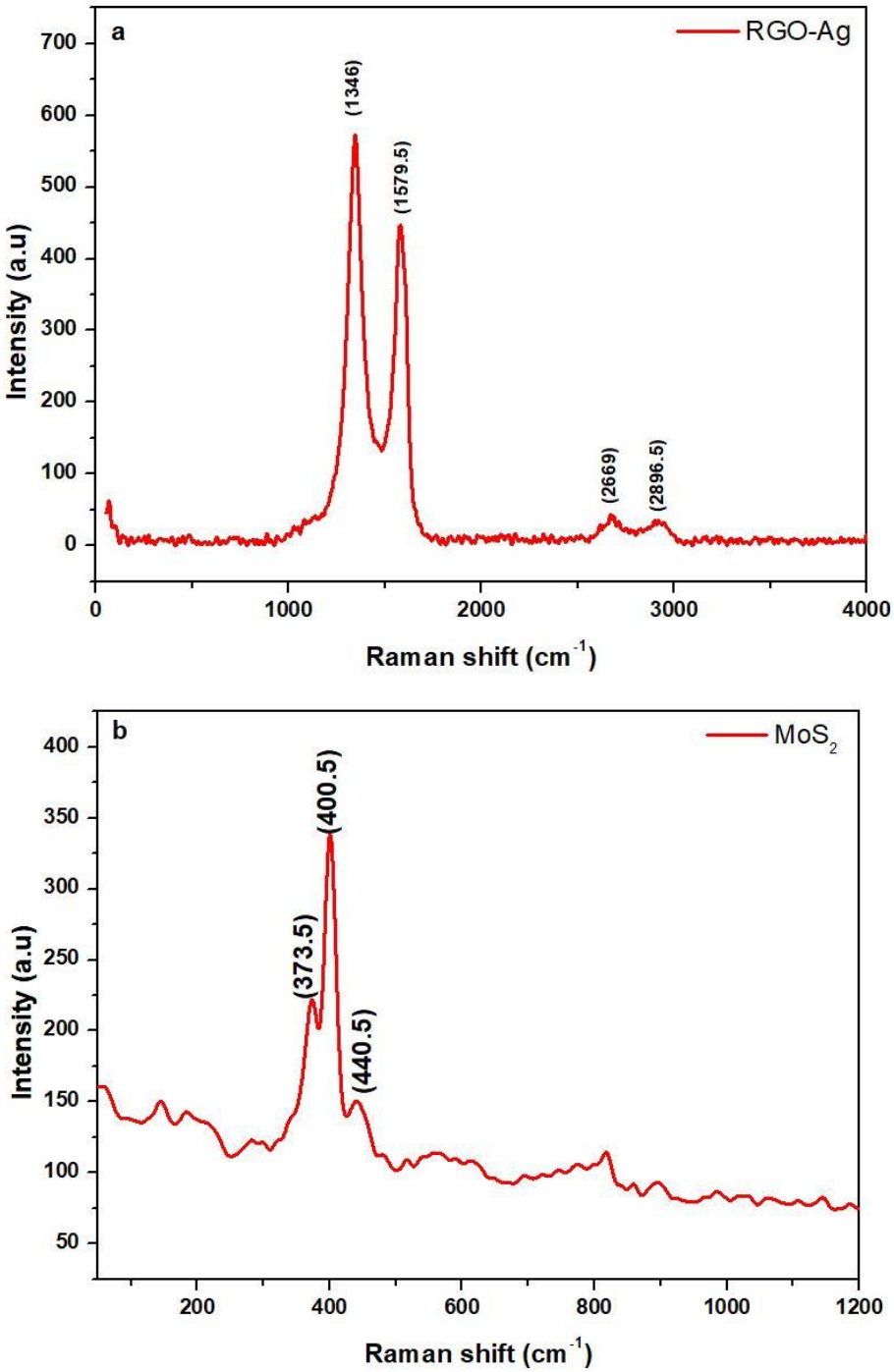

Figure 3. Raman spectrum of synthesized: (a) RGO-Ag, (b) MoS_2.

Figure 4(a) and (b) represents the RGO-Ag surface morphology using SEM. The spreading of AgNPS in the RGO-Ag could be observed. The existence of AgNPS spreading in the RGO matrix stops the piling up of the nanosheets. The AgNPS is consistently dispensed and intercalated RGO nanosheets which enhance the electrical performance of prepared material and increase available electrochemical active sites. Figure 4(c) and (d) demonstrates TEM images of RGO-Ag. Remarkably, the RGO-Ag exhibited numerous AgNPs moored to the surfaces of RGO sheets. AgNPs are deposited on RGO nanosheet are randomly distributed on the RGO surface as a spacer between neighbouring layers [26].

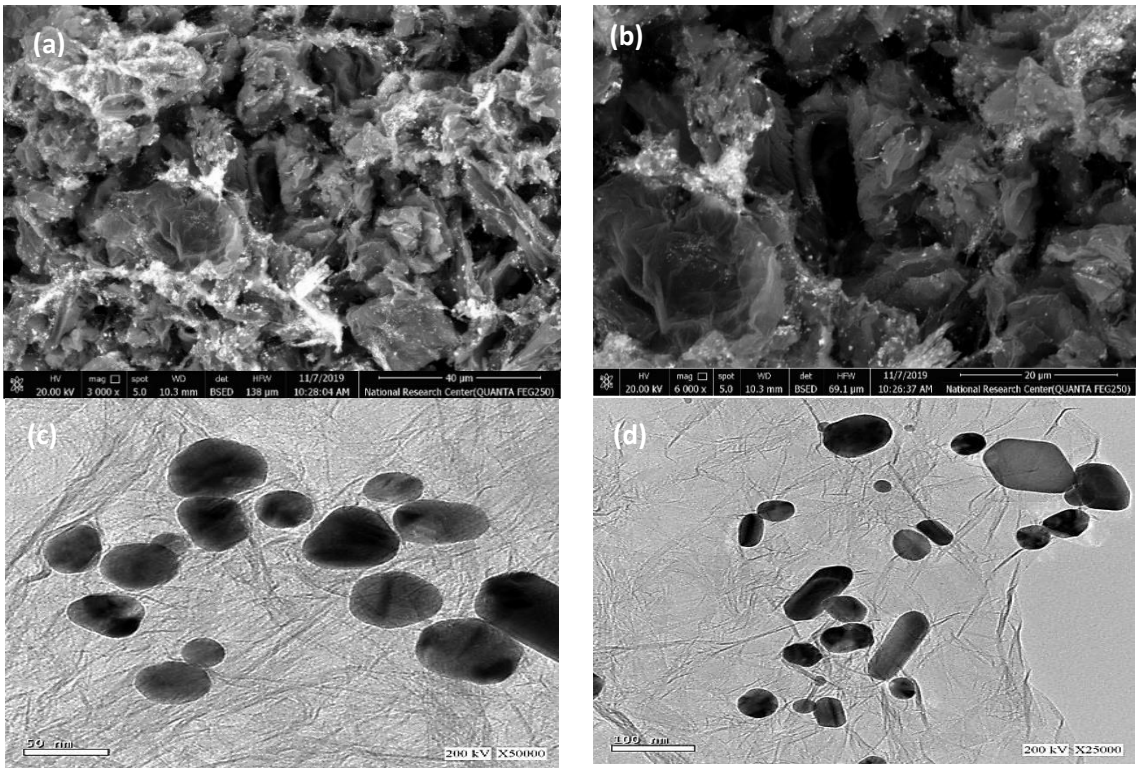

Figure 4. RGO-Ag at different magnification scales: (a) and (b) SEM images; (c) and (d) TEM images.

Figure 5(a) exhibits the SEM image of the synthesized MoS_2, which demonstrates that the prepared MoS_2 consists of microspheres with flower-like. Figure 5(b) provides a perfect vision of the MoS_2 surface morphology. Many nanosheets have been growing on the surface of MoS_2 microspheres then form the flower-like structure during the hydrothermal process [33]. For further disclose the morphology and microstructure of MoS_2 microspheres, TEM measurements were carried out on MoS_2. Figure 5(c) presents the TEM image of MoS_2 where the obvious layered structure could be observed, which prompting the surface area and electronics properties as expected form a 2D material. For better inspection, high-resolution TEM was performed. Figure 5(d) illustrates a few layers MoS_2 with an interlayer spacing of about 0.63 nm which confirms XRD results.

Energy-dispersive X-ray spectrum (EDX) elemental analysis presents the percentage of the most common values of the constituent elements. Figure 6(a) shows the EDX spectrum of synthesized RGO-Ag which affirms the strong signs of three main elements carbon, oxygen, and silver. Their atomic and weight ratios are tabularized and displayed inside the figure. The weight ratio of oxygen element present in the RGO–Ag is very low when compared with the weight ratio of carbon and silver element, which denote the elimination of oxygen functional group from the GO during the formation RGO–Ag and reduction of GO to RGO nanosheets which will improve the electrochemical property of RGO–Ag nanocomposites. Figure 6(b) demonstrates that the prepared MoS_2 consists mainly of Mo and S. The compositional data of the EDX showed the atomic present ratio of Mo and S was 1:3.2, showing that the sulphur atoms were enriched on the MoS_2 ultrathin nanosheets surface.

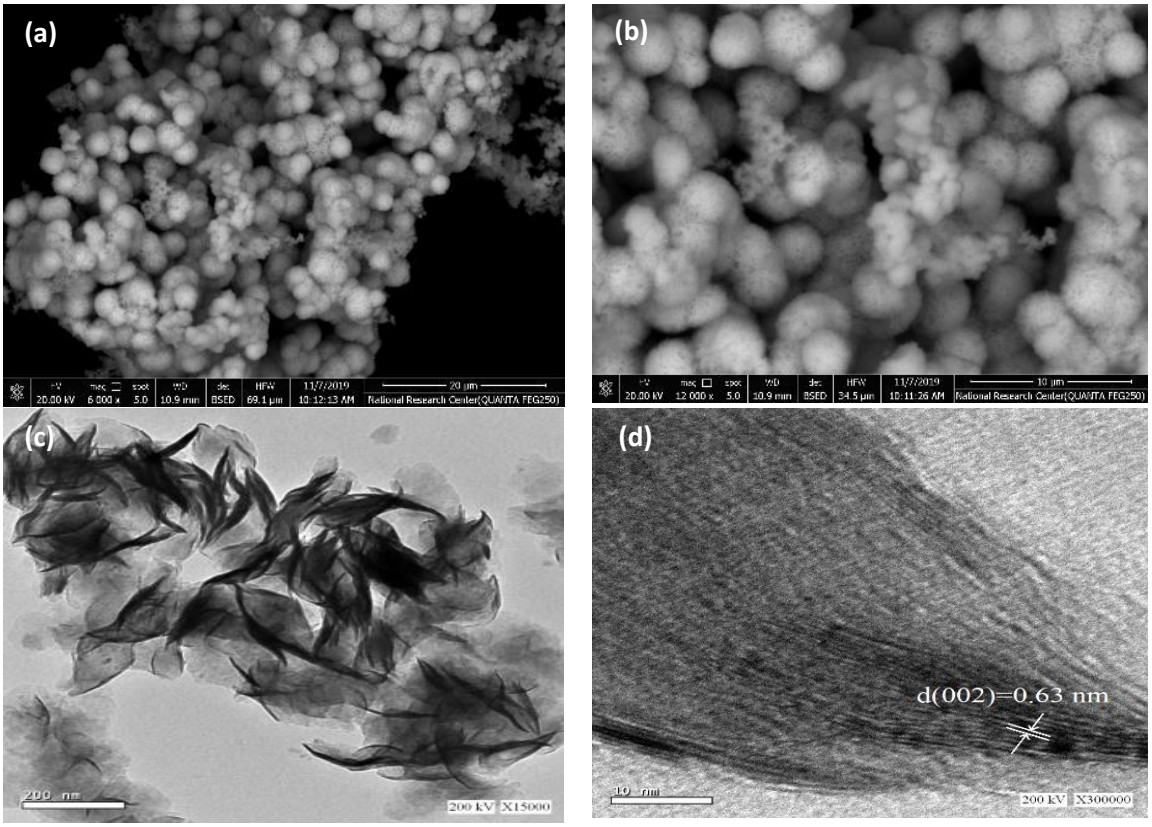

Figure 5. MoS_2 at different magnification scale: (a) and (b) SEM images; (c) and (d) TEM images.

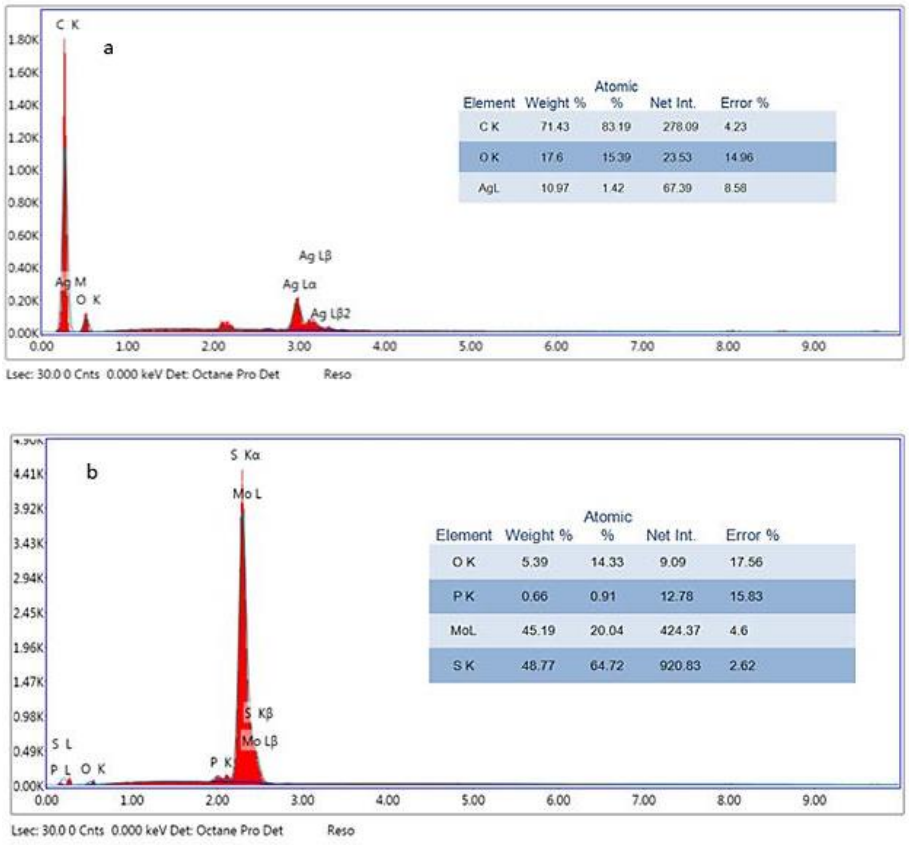

Figure 6. EDX elemental analysis: (a) RGO-Ag, and (b) MoS_2.

3.2 Electrochemical Analysis

The typical CV curves of the prepared symmetric SCs with different electrolytes are displayed in Figure 7(a), 7(b), and 7(c). The three electrolytes exhibited nearly rectangle shape, which gives a good indication of the mechanism of charge storage [34]. For all electrolytes, the SCs show that they have a pseudocapacitive along with electric double layer (EDL) capacitive behaviour.

The non-faradaic process behaviour might be due to the formation of EDL at the electrode/electrolyte interface during the adsorption of protons or cations on the surface of the prepared electrode.

$$(MoS_2)_{surface} + B^+ (K^+ \text{ or } Na^+ or\ Li^+) + e^- \leftrightarrow (MoS_2 - B^+)_{\text{surface}} \quad (3)$$

The pseudocapacitive behaviour would be owing to the faradaic reaction. Ions such as cations of metal alkali (K^+ or $Na^+ or$ Li^+) might prevail inside the interlayer of MoS_2 structure during the redox process.

$$MoS_2 + B^+ + e^- \leftrightarrow MoS - SB^+ \quad (4)$$

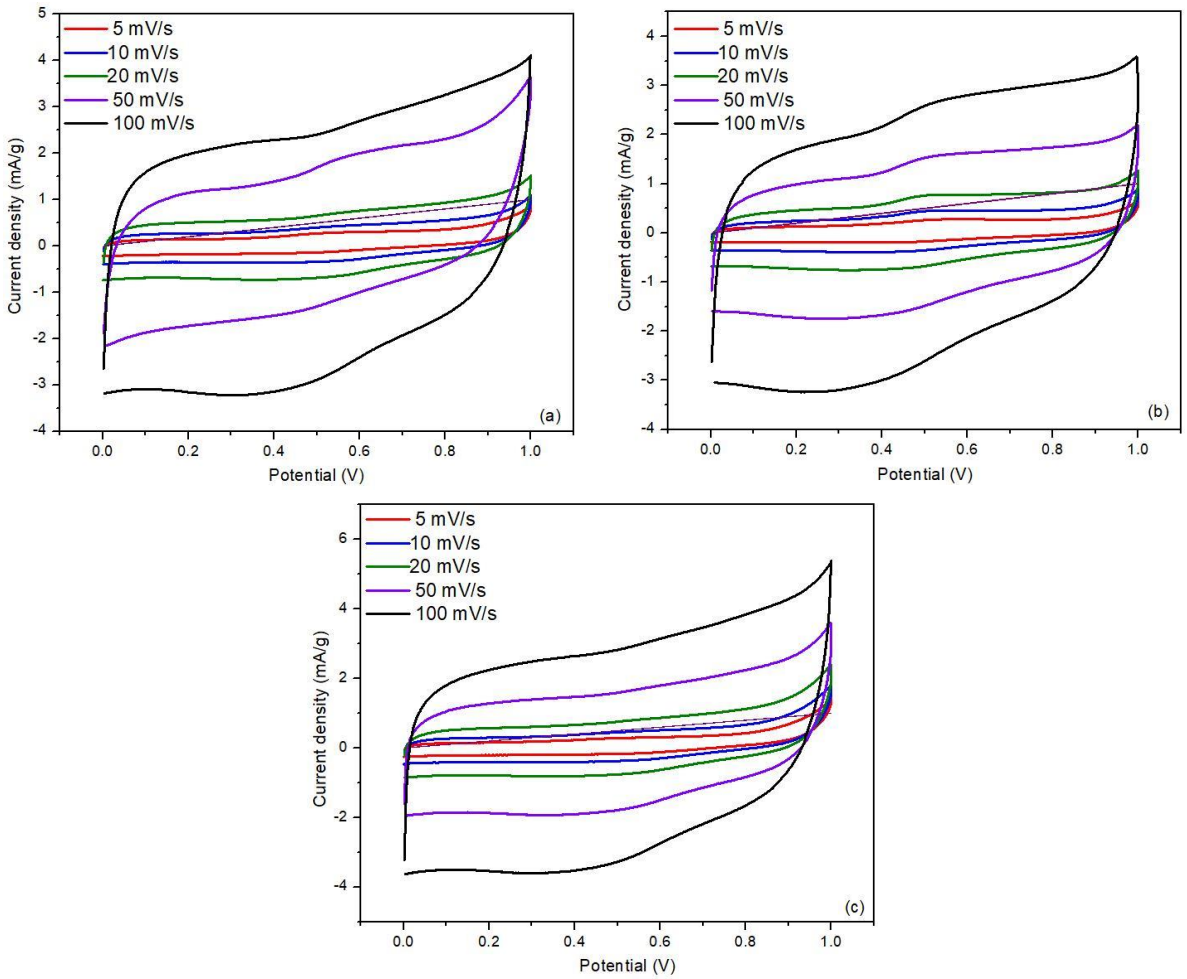

Figure 7. CV curves of the different electrolytes at various scan rates of (a) NaOH, (b) LiOH, and (c) KOH.

The calculated C_{sp} from CV curves is listed in Table 1. It can be detected that the value of C_{sp} reduces with the rise of the scan rate which could be expounded as follow: the high rate of charge/discharge process correlating with a quick rise in the ion concentration in the

electrode/electrolyte interface, which stops the intercalation and motion of ions to inside the electrode which can be attributed to the high scan rate. The efficient interaction between the ions and the electrode considerably decreases as the rate of scan rate rises owing to the increasing resistance of the electrode. Moreover, as the scan rate increases the electrolytic ions do not have enough time to interrelate well with the active material of the electrode. The prepared SC exhibited a capacitance that relies on the electrolyte used as KOH > NaOH > LiOH. The hydrated radius of K^+, Na^+, and Li^+ are 3.31, 3.58, and 3.82 Å, respectively. The highest ionic conductivity and the smallest hydrated ionic radius of K^+ make its entree to the inner surface of the MoS_2 active material is easier and quicker than that of Na^+ and Li^+. Therefore the specific capacitance of the prepared symmetric SC with KOH electrolyte is higher than the two other electrolytes [35].

Table 1 The specific capacitance for three electrolytes at various scan rates

Scan rate ($mv.s^{-1}$)	Specific capacitance (C_{sp}) $F.g^{-1}$		
	Electrolyte		
	NaOH	**LiOH**	**KOH**
5	133	120.26	171
10	111.72	106.64	137.06
20	103.292	96.68	119.87
50	89.86	83.78	102.14
100	83.3152	73.49	90.97

The specific capacitance of fabricated SCs has been also estimated by the GCD technique. The GCD curves of the symmetric two electrodes system for three electrolytes were obtained using different current densities (0.2- 10 $A.g^{-1}$). Figure 8(a), (b), and (c) present nearly triangular shapes of charge accumulation with voltage. For all electrolytes, the voltage drop at the beginning of discharge was imputed to the inner resistance of the MoS_2 active material. It is noted that the voltage drop at the beginning has a very low value even at the high current densities, demonstrating fast response and small internal resistance of the SC. The SC with KOH electrolyte shows the longest time of discharge, demonstrating the highest value of C_{sp} when compared with the two other electrolytes. This result matched with the result presented in the CV curves in Figure 7(c). The specific capacitance as a function of the scan rate for the three SCs is present in Figure 8(d). The SC with KOH electrolyte presents a high specific capacitance of 137.93 $F.g^{-1}$ at 0.2 $A.g^{-1}$. As the current density increases 50 times of 10 A. g^{-1}, it retains 19.77 $F.g^{-1}$.

The energy density (ED) and the power density (PD) are very significant parameters for SC evaluation to determine the performance and the efficiency of operation of the prepared SCs. The ED and PD are evaluated from GCD based on the unit mass of active material by Eq. (5) and Eq. (6), respectively:

$$\mathrm{E}D = \frac{Cs(\Delta V)^2}{7.2} \tag{5}$$

$$PD = \frac{ED}{\Delta t} \tag{6}$$

Where ΔV, Δt are the voltage window and the required time to discharge the SC, respectively. The power density and the corresponding energy density for the three SCs are plotted in the Ragone plot shown in Figure 9 (a). The associated three electrolytes show a high-power density up to 20 $KW.Kg^{-1}$ at current density 10 $A.g^{-1}$.

The good electrochemical performance of MoS_2 microspheres can be imputed to the unique structure that provides a high specific surface area, a shorter channel for ion transition, the existence of ultrathin MoS_2 sheets that provide more active sites for redox reactions. The use of 10 % of RGO-Ag as a conductive additive enhanced the electrical conductivity and capacitive performance as well. Moreover, RGO-Ag promoted the migration of electrolyte ions through the electrode.

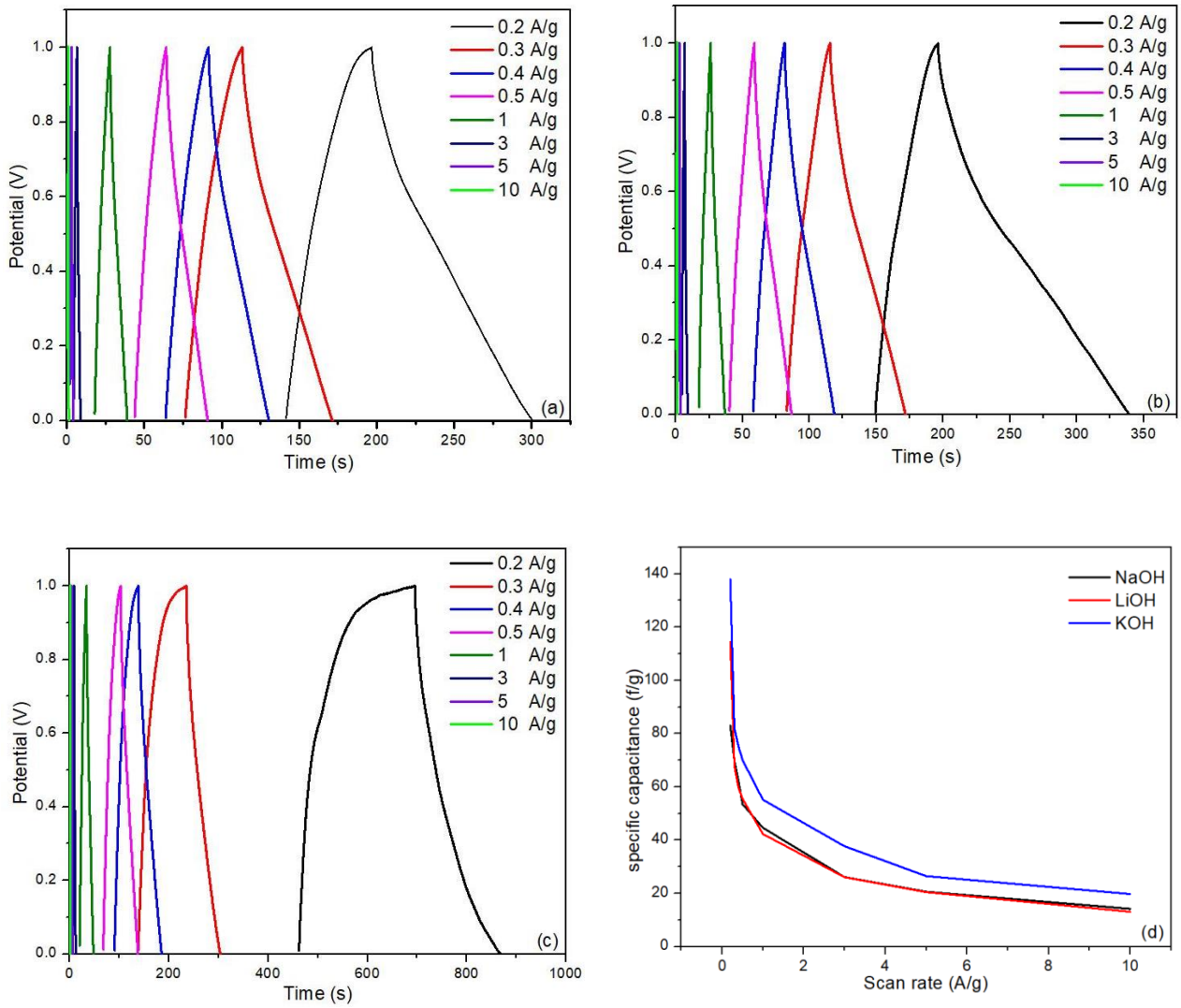

Figure 8. The second cycle of galvanostatic charge/discharge curves of different electrolytes at various current densities of (a) NaOH, (b) LiOH, and (c) KOH. (d) The rate capability of the SC at different scan rates for the three electrolytes.

Electrochemical Impedance Spectroscopy (EIS) is an electrochemical characterization technique where the response of electrodes is in the form of AC signals at different frequencies. EIS was further used to investigate the impedance in a two-electrode system. The equivalent circuit model in Figure 9(b) was utilized for fitting the investigational EIS data.

The Nyquist plot of the prepared SC with different electrolytes is presented in Figure 9(c), (d), and (e). The low-frequency domain demonstrates an ideal behaviour with rapid ion diffusion owing to the specific structure of the MoS_2 microsphere that is convenient for the rapid movement of electrolyte ions. The semicircle in the high frequency domain is imputed to the electrolyte

resistance and the straight line is correlated with the diffusive resistance. The value of electrolyte resistance (R_1) and diffusion resistance (R_2) for the three electrolytes are presented in Table 2

Table 2 The electrolyte resistance (R_1) and diffusion resistance (R_2) for the three electrolytes

Resistance (Ω)	**KOH**	**LiOH**	**NaOH**
electrolyte resistance (R_1)	0.76	0.817	0.846
diffusion resistance (R_2)	5.95	4.122	4.034

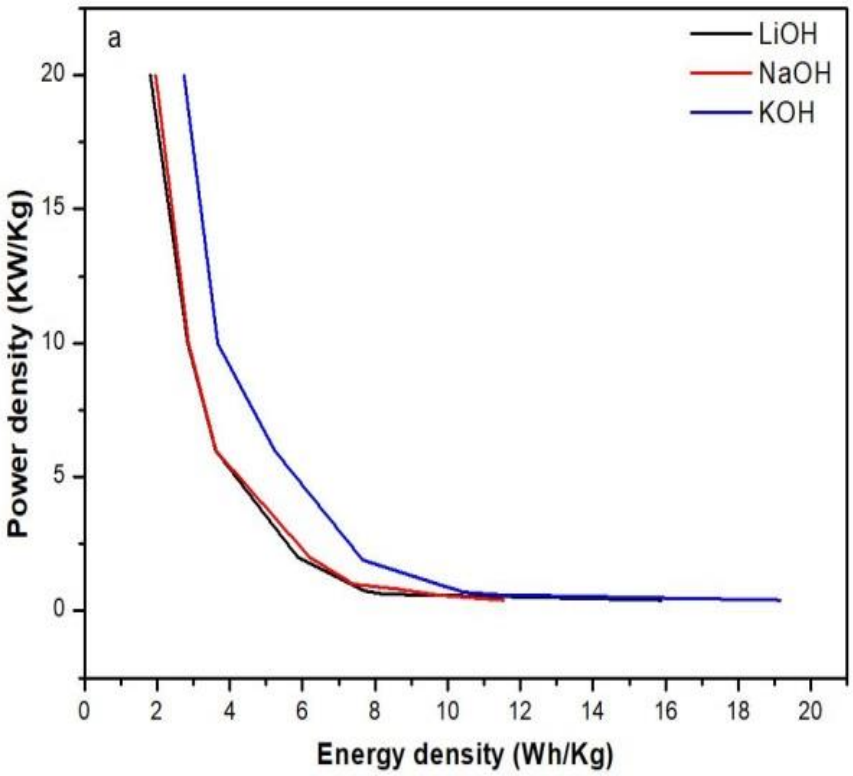

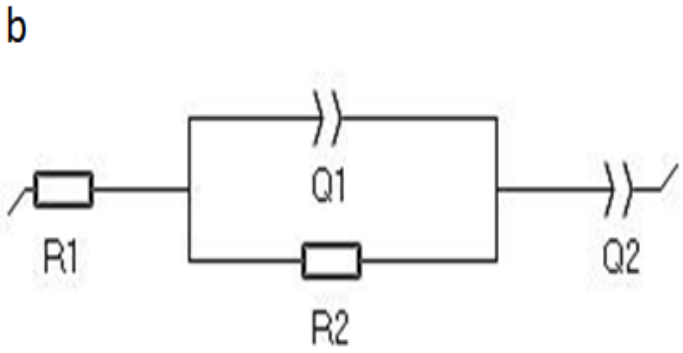

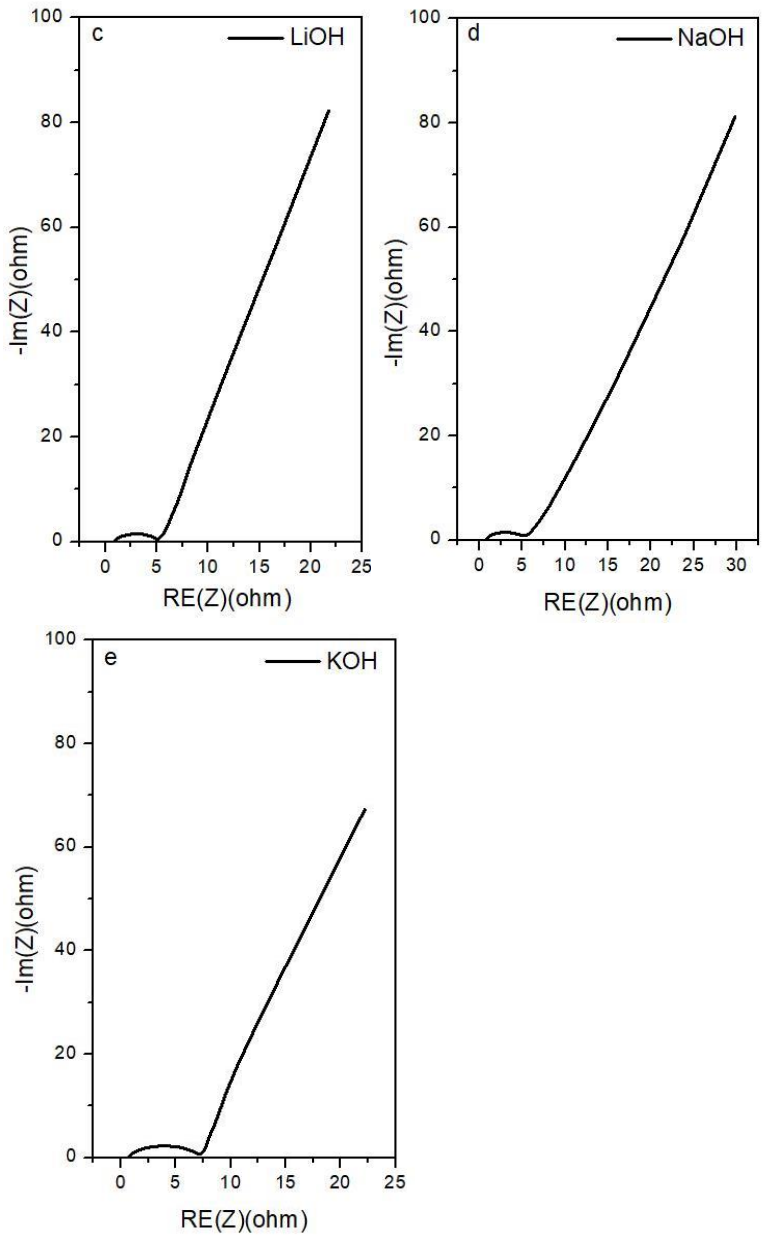

Figure 9. (a) Ragone plot curves of different electrolytes at various energy densities, (b) The EIS equivalent circuit and Nyquist plot of (c) LiOH, (d) NaOH, and (e) KOH.

Cyclic stability is one of the most significant properties for the actual applications of ESDs. Figure 10(a) shows the capacitive retention of the fabricated SC in 5M KOH, 5M NaOH, and 5M LiOH electrolytes after 1000 cycles at the scan rate of 1 $A.g^{-1}$ calculated using GCD test. It was clearly observed that the fabricated devices with three electrolytes possess capacitance retention of 98.5%, 96%, and 82%, respectively. The cause of this difference was studied, and it was found that the internal resistance gradual increase might be imputed to the imperfect reversal of the faradaic process during the discharge process. Consequently, maintain the retention rate of the SCs at such levels [36]. On the other hand, LiOH and NaOH provide a good indication of the prepared MoS_2 stability in alkaline mediums. Long term cyclic stability of 12000 cycles retention at 10 $A.g^{-1}$ test was applied for both LiOH and NaOH. Figure 10(b) presents the long-term retention of LiOH and NaOH. Remarkably, the LiOH based SC restricted on 90.3 % value while NaOH restricted on 87.4%.

Table 3 presents previous reports of MoS_2 based SCs compared to this work results and shows the enhancement over many reported two electrodes configuration. The two electrodes configuration is typically utilized to characterize the full packaged SCs, while the three-electrode system is useful for investigating the essential electrochemical advantages of the electrode material. The value of C_{sp} gotten from the two-electrode configuration will be about four times smaller than that of the three-electrode. Therefore, the two electrodes outcomes cannot be compared with three-electrodes results [25]. The possibility of existences of P-N junctions cause increase in the active site of the electrode material, which allows more electrons to participate in the reaction. This has a considerable effect on enhancing the electrochemical performance of this work [37].

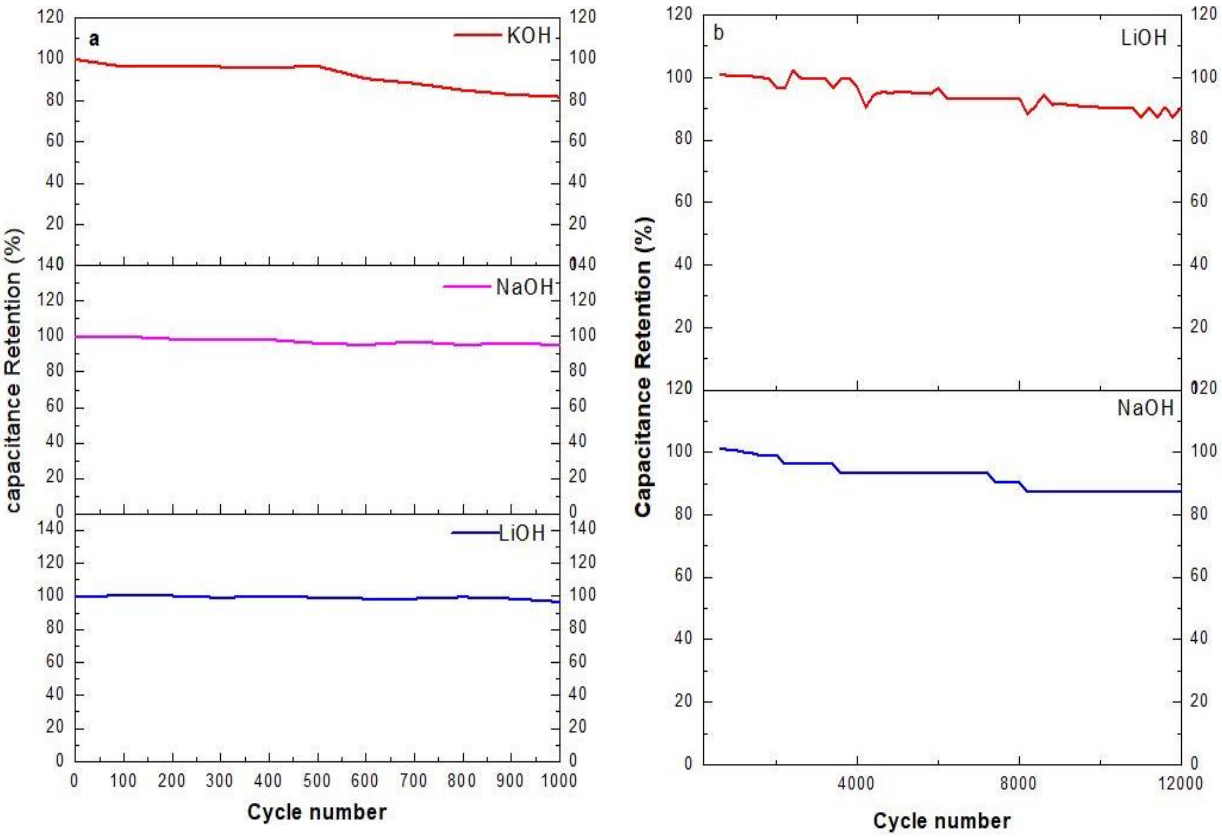

Figure 10; (a) Cycle stabilities of different electrolytes for 1000 cycles at 1A.g^{-1} and (b) Long term Cycle stability of LiOH and NaOH for 12000 cycles at 10 A.g^{-1}.

Table 3 Comparison of electrochemical properties of SC based on different MoS_2 electrode materials

Material	Electrolyte	C_{sp} (F/g)	ED (Wh/kg)	PD (W/kg)	Configuration	Retention	Ref.
MoS_2 nanosheets	1 M Na_2SO_4	129.2	-	-	Three electrodes	85.1% (500 cycle)	[38]
Sphere like MoS_2	1 M Na_2SO_4	106	7.25	186.5	Three electrodes	93.8% (1000 cycle)	[39]
Spherically clustered MoS_2	1 M H_2SO_4	113	17	204	Three electrodes	-	[40]
Hollow MoS_2 nanospheres	1 M KCl	142	-	-	Three electrodes	92.9% (1000 cycle)	[41]

MoS_2 monolayers	6 M KOH	366.9	-	-	Three electrodes	92.2% (1000 cycle)	[42]
flower-like MoS_2 nanostructures	1M Na_2SO_4	168	-	-	Three electrodes	92.6% (3000 cycles)	[43]
Microspheres MoS_2	3M KOH	346	5	1200	Three electrodes	80% (5000 cycles)	[44]
MoS_2 Nanowall	0.5M H_2SO_4	100	-	-	Three electrodes	-	[45]
Microspheres MoS_2	1 M KOH	68.9	21.3	750	Two electrodes	92% (3000 cycles)	[46]
MoS_2 Nanosheets	1 M KOH	69	-	-	Three electrodes	87% (1000 cycles)	[47]
Hexagonal MoS_2	2M KOH	172	-	-	Three electrodes	72.4 % (2000 cycles)	[48]
1T/2H MoS_2 Microspheres	0.5M K_2SO_4	79.4	1.5	4500	Two electrodes	72% (2000 cycles)	[49]
Flower-like MoS_2 microspheres	5 M LiOH	120.26	1.813	~20000	Two electrodes	90.3 (12000 cycles)	**This work**

4. CONCLUSION

In summary, MoS_2 microspheres were synthesized by a facile and low-cost hydrothermal approach. The capacitive properties of the symmetric prepared SCs based on MoS_2 and RGO-Ag as the conductive agent were studied with three different alkaline hydroxide electrolytes which are KOH, LiOH, and NaOH. The results demonstrate that the RGO-Ag improves the conductivity of electrodes resulting in enhanced capacity, cycling performance, and rate capabilities of the cells. The electrochemical measurements indicate that the fabricated SC with LiOH exhibited a high specific capacitance of about 120 $F.g^{-1}$ at a 5 $mV.s^{-1}$ scan rate. Furthermore, a high-power density of about 20 $KW.kg^{-1}$ at 10 $A.g^{-1}$ as well as good long-term cycling stability of 90.3 % over 12000 cycles in a two-electrode cell. The good capacitance performance could be attributed to the following; (i) using All-2d-active materials, (ii) the synergistic effect with using RGO-Ag, (iii) the composite P-N junction formation due to mixing RGO-Ag as p-type and MoS_2 as the n-type and (iv) using alkaline electrolytes with high electrochemical affinity. Accordingly, these promising results propose that the MoS_2 can be utilized as a highly efficient electrode material for SC applications.

REFERENCES

[1] N.L. Panwar, S. C. Kaushik, S. Kothari, Renew. Sustain. Energy Rev. **15** (2011) 1513–1524.
[2] M. Wang, H. Zhang, C. Wang, X. Hu, G. Wang, Electrochim. Acta. **91** (2013) 144–151.
[3] A. M. Abd Elhamid, H. Shawkey, A. A. Nada, M. Bechelany, Solid State Sci. **94** (2019) 28–34.
[4] L. Li, Z. Wu, S. Yuan, X. B. Zhang, Energy Environ. Sci. **7** (2014) 2101–2122.
[5] Z. S. Iro, C. Subramani, S. S. Dash, Int. J. Electrochem. Sci. **11** (2016) 10628–10643.
[6] L. L. Zhang, X. S. Zhao, Chem. Soc. Rev. **38** (2009) 2520–2531.
[7] A. A. Alamin, A. M. Abd Elhamid, W. R. Anis, A. M. Attiya, Diam. Relat. Mater. **96** (2019) 182–194.
[8] H. Hwang, H. Kim, J. Cho, Nano Lett. **11** (2011) 4826–4830.
[9] N. Choudhary, M. Patel, Y.-H. Ho, N.B. Dahotre, W. Lee, J.Y. Hwang, W. Choi, J. Mater. Chem. A. **3** (2015) 24049–24054.
[10] E. G. Da Silveira Firmiano, A. C. Rabelo, C. J. Dalmaschio, A. N. Pinheiro, E. C. Pereira, W. H. Schreiner, E.R. Leite, Adv. Energy Mater. **4** (2014) 1301380.
[11] R. Wang, S. Wang, X. Peng, Y. Zhang, D. Jin, P.K. Chu, L. Zhang, ACS Appl. Mater. Interfaces. **9** (2017) 32745–32755.

[12] J. Zhu, W. Sun, D. Yang, Y. Zhang, H. H. Hoon, H. Zhang, Q. Yan, Small. **11** (2015) 4123–4129.
[13] N. Li, T. Lv, Y. Yao, H. Li, K. Liu, T. Chen, J. Mater. Chem. A. **5** (2017) 3267–3273.
[14] M. A. Bissett, I. A. Kinloch, R. A. W. Dryfe, ACS Appl. Mater. Interfaces. **7** (2015) 17388–17398.
[15] X. Li, C. Zhang, S. Xin, Z. Yang, Y. Li, D. Zhang, P. Yao, ACS Appl. Mater. Interfaces. **8** (2016) 21373–21380.
[16] J. Wang, Z. Wu, K. Hu, X. Chen, H. Yin, J. Alloys Compd. **619** (2015) 38–43.
[17] K.-J. Huang, L. Wang, Y.-J. Liu, H.-B. Wang, Y.-M. Liu, L.-L. Wang, Electrochim. Acta. **109** (2013) 587–594.
[18] B. E. Conway, Scientific fundamentals and technological applications, B. Electrochem. Supercapacitors, (2013) 528.
[19] C. Portet, G. Yushin, Y. Gogotsi, Carbon N. Y. **45** (2007) 2511–2518.
[20] S. Zhang, C. Lum, N. Pan, Nanotechnol. Environ. Eng. **2** (2017) 9.
[21] B. Alemour, M. H. Yaacob, H. N. Lim, M. R. Hassan, Int. J. Nanoelectron. Mater. **11** (2018).
[22] M. Abd Elhamid, A. A. Alamin, A. M. Selim, M. A. Wasfey, M. B. Zahran, Int. Conf. Adv. Control Circuits Syst. 2019 5th Int. Conf. New Paradig. Electron. Inf. Technol., IEEE, (2019) 151–155.
[23] A. H. Surani, A. R. A. Rashid, N. Arshad, A. A. N. Hakim, Int. J. Nanoelectron. Mater. **12** (2019).
[24] C.Y. Fu, S. Xing, T. Shen, B. Tai, Q.M. Dong, H.B. Shu, P. Liang, Wuli Xuebao/Acta Phys. Sin. **64** (2015) 2022–2024.
[25] M. D. Stoller, R.S. Ruoff, Energy Environ. Sci. **3** (2010) 1294–1301.
[26] S. Gurunathan, J. W. Han, J. H. Park, E. Kim, Y. J. Choi, D. N. Kwon, J. H. Kim, Int. J. Nanomedicine. **10** (2015) 6257–6276.
[27] Z. Zhang, F. Xu, W. Yang, M. Guo, X. Wang, B. Zhang, J. Tang, Chem. Commun. **47** (2011) 6440–6442
[28] L. Luo, M. Shi, S. Zhao, W. Tan, X. Lin, H. Wang, F. Jiang, J. Saudi Chem. Soc. **23** (2019) 762–773.
[29] S. Thakur, N. Karak, Carbon N. Y. **50** (2012) 5331–5339.
[30] M.S. Dresselhaus, A. Jorio, M. Hofmann, G. Dresselhaus, R. Saito, Nano Lett. **10** (2010) 751–758.
[31] B. C. Windom, W. G. Sawyer, D. W. Hahn, Tribol. Lett. **42** (2011) 301–310.
[32] G. Plechinger, S. Heydrich, J. Eroms, D. Weiss, C. Schüller, T. Korn, Appl. Phys. Lett. **101** (2012) 101906.
[33] X. Zhang, X. Huang, M. Xue, X. Ye, W. Lei, H. Tang, C. Li, Mater. Lett. **148** (2015) 67–70.
[34] Y. Gogotsi, R.M. Penner, Energy storage in nanomaterials–capacitive, pseudocapacitive, or battery-like? (2018).
[35] H. Friedman, Ionic hydration in chemistry and biophysics, Elsevier Amsterdam, (1982).
[36] D. Guragain, C. Zequine, R. K. Gupta, S. R. Mishra, Processes. **8** (2020) 3182–3194.
[37] W. Shang, Y. Tan, L.-B. Kong, F. Ran, ACS Appl. Mater. Interfaces. (2020).
[38] K. J. Huang, J. Z. Zhang, G. W. Shi, Y. M. Liu, Electrochim. Acta. **132** (2014) 397–403.
[39] K. Krishnamoorthy, G.K. Veerasubramani, S. Radhakrishnan, S. J. Kim, Mater. Res. Bull. **50** (2014) 499–502.
[40] P. Ilanchezhiyan, G. Mohan Kumar, T. W. Kang, J. Alloys Compd. **634** (2015) 104–108.
[41] L. Wang, Y. Ma, M. Yang, Y. Qi, Electrochim. Acta. **186** (2015) 391–396.
[42] L. Jiang, S. Zhang, S.A. Kulinich, X. Song, J. Zhu, X. Wang, H. Zeng, Mater. Res. Lett. **3** (2015) 177–
[43] X. Wang, J. Ding, S. Yao, X. Wu, Q. Feng, Z. Wang, B. Geng, J. Mater. Chem. A. **2** (2014) 15958–15963.
[44] H. Adhikari, C. Ranaweera, R. Gupta, S. R. Mishra, MRS Adv. **1** (2016) 3089–3097.
[45] J. M. Soon, K. P. Loh, Electrochem. Solid-State Lett. **10** (2007) 250–254.
[46] N. Joseph, P. Muhammed Shafi, A. Chandra Bose, New J. Chem. **42** (2018) 12082–12090.
[47] D. Liang, Z. Tian, J. Liu, Y. Ye, S. Wu, Y. Cai, C. Liang, Electrochim. Acta. **182** (2015) 376–382.
[48] D. Wang, Y. Xiao, X. Luo, Z. Wu, Y.J. Wang, B. Fang, ACS Sustain. Chem. Eng. **5** (2017) 2509–2515.

[49] B. A. Ali, A. M. A. Omar, A. S. G. Khalil, N. K. Allam, ACS Appl. Mater. Interfaces. **11** (2019) 33955–33965.